Peer-reviewed version available at Remote Sens. 2020, 12, 446; doi:10.3390/rs12030446

Article

A New Potential of the Deep Convective Clouds as the Calibration Target for a Geostationary UV/VIS Hyperspectral Spectrometer

Yeeun Lee[1], Myoung-Hwan Ahn[1],* and Mina Kang[2]

[1] Department of Climate and Energy Systems Engineering, Ewha Womans University, 52 Ewhayeodae-gil, Seodaemun-gu, Seoul 03760; yeenylee@gmail.com
[2] Department of Atmospheric Science and Engineering, Ewha Womans University, 52 Ewhayeodae-gil, Seodaemun-gu, Seoul 03760; agewha@naver.com
* Correspondence: terryahn65@ewha.ac.kr; Tel.: +82-3277-4462

Abstract: As one of GEO-constellation for environmental monitoring in the next decade, Geostationary Environment Monitoring Spectrometer (GEMS) is designed to observe the Asia Pacific region to provide the information on the atmospheric chemicals, aerosol and cloud properties. For the continuous monitoring of the sensor performance after its launch in early 2020, here we suggest deep convective clouds (DCCs) as a possible target for the vicarious calibration of GEMS, the first UV/VIS hyperspectral sensor onboard a geostationary satellite. Tropospheric Monitoring Instrument (TROPOMI) and Ozone Monitoring Instrument (OMI) are used as a proxy of GEMS, and a conventional DCC detection approach applying the thermal threshold test is used for the DCC detection based on the collocations with Advance Himawari-8 Imager (AHI) onboard Himawari-8 geostationary satellite. DCCs are frequently detected over the GEMS observation area on average over 200 pixels in a single observation scene. Considering the spatial resolution of GEMS, 3.5 km×7 km which is similar to TROPOMI, and its temporal resolution (8 times a day), availability of DCCs for vicarious calibration of GEMS is expected to be sufficient. Inspection of the DCC reflectivity spectra estimated from the OMI and TROPOMI data also shows a promising result. Even though, their observation geometry and sensor characteristics are quite a different, the estimated DCC spectra agree quite a well within a known uncertainty range with comparable spectral features. When the DCC detection is further improved by applying both visible and infrared tests, the variability of DCC reflectivity from the TROPOMI data is reduced by half, from 10% to 5%. This is mainly due to the efficient screening of cold thin cirrus with the visible test and of bright warm clouds with the infrared test. The precise DCC detection is also expected to contribute to the accurate characterization of the cloud reflectivity, which will be further investigated.

Keywords: GEMS; UV; VIS; hyperspectral data; deep convective cloud; vicarious calibration, OMI, TROPOMI

---

1. Introduction

With the global transport of anthropogenic chemicals in the atmosphere becoming a controversial issue over recent years, satellite has been considered as one of key measures to keep track of the chemicals with its large spatial coverage. In the Asia-Pacific region, Geostationary Korea Multi-Purpose Satellite-2B (GEO-KOMPSAT-2B, GK-2B) is expected to perform such a role after its launch planned in February 2020 with an ultraviolet (UV) and visible (VIS) hyperspectral sensor, Geostationary Environment Monitoring Spectrometer (GEMS). GEMS is designed to observe the Asia Pacific region including the Korea Peninsula and its surrounding area to continuously monitor the atmospheric conditions by retrieving concentration of atmospheric chemicals and aerosol properties [1,2]. For the consistency of the measurements, on-board calibration with solar diffusers and light-emitting diode (LED) are deployed in the GEMS calibration system which converts the light from the

Peer-reviewed version available at *Remote Sens.* **2020**, *12*, 446; doi:10.3390/rs12030446

scene to the calibrated spectral data (level-1B). However, it has been frequently reported in the previous satellite programs that the residual errors in the level-1B data introduce some level of uncertainty to the higher level products [3–8]. It is also highly probable that the sensor characteristics might be changed over time by both internal and external factors and this makes it necessary for a sensor to be continuously monitored and calibrated.

Vicarious calibration is one of well-known approaches for monitoring and improving the sensor performance by periodically comparing with the reference targets. To successfully perform the calibration, it is important to select a proper target which is stable enough to be repeatedly observed and well-characterized under the different observation conditions. Because of these requirements, some particular observation targets have been used for the calibration such as snow and ice over polar region, bright clouds, desert and artificial sites [9–14]. Among the targets, however, there is a limitation for the geostationary earth orbit (GEO) sensor since the sensor only covers a particular spatial region while the low-earth orbit (LEO) sensor covers the entire surface of the Earth. Since GEMS only measures UV and VIS radiances reflected by the atmosphere and earth's surface, their variation also imposes a limit for a stable target.

Deep convective clouds (DCCs), in this respect, is an excellent candidate as a calibration target for GEMS considering their physical and radiative properties. DCCs are the clouds frequently observed over the tropical western Pacific (TWP) region with their tops reaching nearly up to or over the tropopause due to the strong vertical convection [15–18]. This means that the backscattered radiation from the cloud is less affected by the Earth's surface and the troposphere where most of the atmospheric constituents reside. Reflective properties of the cloud top also have been fairly well characterized with its spatially uniform and less penetrative features especially in the VIS and infrared (IR) spectral region [19–22]. With these characteristics, DCCs have been widely used as the reference target for the monitoring of the VIS and IR satellite sensors [23–31]. However, little attention has been paid to the applicability of DCCs as the reference targets in the UV spectral region since there are not many UV sensors especially onboard a GEO satellite. In this study, we aim to present the applicability of the DCCs as the reference target for GEMS, the UV-VIS spectrometer onboard the GEO satellite. Some of the advantages using the DCCs as the target are still valid even at the shorter wavelengths, for instance, weaker dependence on the atmospheric condition, distinct brightness of the clouds as well as little spectral dependence in the cloud reflectivity [32].

To select only spatially homogeneous clouds, we apply an DCC detection routine with IR brightness temperature (TB) threshold suggested by Doelling et al. [27] as well as an adaption of the UV-VIS threshold. Combining the thermal and reflective signal is expected to provide a better chance of selecting desirable DCCs since each radiative property gives different information on the cloud [33,34]. To evaluate the applicability of the DCC calibration, in Section 2, we firstly check whether the DCCs occur over the TWP region with enough numbers that could provide a reliable statistical parameters. As GEMS does not cover the IR region, we use the TB and reflectivity data from the Advanced Himawari Imager (AHI) onboard the geostationary weather satellite (Himawari-8) to derive a simple climatology of DCCs over the TWP region. After checking the sufficient occurrence of DCCs over the TWP region, UV-VIS hyperspectral data of OMI onboard Aura and Tropospheric Monitoring Instrument (TROPOMI) onboard Sentinel-5 Precursor (S5P) are used as a proxy of GEMS for the spectral analysis of DCCs. In Section 3, we compare the OMI and TROPOMI DCCs to confirm whether the detected DCCs reflect stable and bright signal enough to reduce the different sensor characteristics as having homogeneous spectral features. Based on the results, in Section 4, DCC detection thresholds are tested to optimize the detection for the further characterization of the cloud reflectivity.

2. Data and Methods

2.1. UV-VIS Hyperspectral Sensor

2.1.1. GEMS

GEMS covers the Asia-Pacific region (5°S-45°N and 75°E-145°E) observing the Earth in the east-west direction with the fixed north-south field of view (FOV) of 7.73° [2]. For the retrieval of the concentrations of atmospheric gases (O_3, NO_2, SO_2 and HCHO) and aerosol properties, GEMS is designed to provide continuous spectrum from 300 to 500 nm with spectral resolution of better than 0.6 nm at every 0.2 nm. As the first hyperspectral UV-VIS sensor onboard GEO satellite, GEMS is expected to provide critical information to monitor the regional transport of atmospheric chemicals at an hourly temporal resolution during the daytime as a part of GEO-constellation [35].

Prior to the launch of the satellite, on-ground sensor characterization and calibration have been conducted in the preparatory phase for GEMS. While in orbit, GEMS relies on the on-board calibration system consisting of solar diffuser and LED to evaluate and maintain calibration quality. As a part of the on-board calibration system, LED serves as a stable light source to check the non-linearity of electronic response and the aliveness of each pixels at the detector-level. Solar measurements are also designed to monitor and calibrate sensor response changes with two transmissive diffusers, a working and reference diffuser. The working diffuser is planned to observe the Sun on a daily basis, yet it is known to be gradually degraded during the entire mission because of the daily exposure to the Sun. Thus, a reference diffuser identical with the former but observing the Sun once every six months is included together in the calibration system. However, since most parts of the sensor are expected to be degraded as time passes, it is important to decompose the degradation from each part of the sensor and properly calibrate the changes. Since the on-board calibration is included in the calibration system, an independent way to evaluate the overall performance of the calibration system could be useful to maintain the data quality for GEMS in the long-term operation as a back-up calibration plan.

2.1.2. OMI and TROPOMI

OMI and TROPOMI are both hyperspectral sensors encompassing the spectral range as well as the observation area of GEMS. Operating in a sun-synchronous polar orbit, both sensors take radiance measurement in the ascending node of the satellites at around the local solar time (LST) of 13:30. The top-level specification of GEMS, OMI and TROPOMI is summarized in Table 1. As newly launched in October 2017, TROPOMI especially has stricter data quality requirements compared to other sensors. Since the spatial and spectral resolution of GEMS is also quite similar to the resolution of TROPOMI, these sensors are highly expected to be reciprocal candidates for the inter-calibration after the operation of GEMS.

Table 1. Sensor specification of GEMS, OMI and TROPOMI

Sensor	**GEMS**	**OMI**		**TROPOMI**	
Orbit type	Geosynchronous (nadir at 128°E)	Sun-synchronous (Mean LST – 13:45)		Sun-synchronous (Mean LST – 13:35)	
Spectral range	300-500 nm	UV-2	307-383 nm	Band3	320-405 nm
		VIS	349-504 nm	Band4	405-500 nm
Spectral resolution	< 0.60 nm	UV-2	0.42 nm	Band3	0.55 nm
		VIS	0.63 nm	Band4	
Spectral sampling	< 0.20 nm/pixel	UV-2	0.14 nm/pixel	Band3	0.20 nm/pixel
		VIS	0.21 nm/pixel	Band4	
Spatial resolution	4.9 × 8 km^2 (at the equator)	13 × 24 km^2 (along × across track)		3.5 × 5.5 km^2 (along × across track)	

Preprints (www.preprints.org) | NOT PEER-REVIEWED | Posted: 19 December 2019 doi:10.20944/preprints201912.0260.v1

Peer-reviewed version available at Remote Sens. 2020, 12, 446; doi:10.3390/rs12030446

2.2. DCC Climatology

To check whether there are enough DCCs available within the GEMS field of regards (FOR) especially over the TWP region, we apply the conventional DCC detection approach, threshold tests for TB and uniformity of the clouds [26]. Threshold values used for each test along with the constraints of observation angles and spatial coverage are summarized in Table 2. For the TB test, we use the 11 µm window channel with the threshold of 205 K which is set considering the trade-off between the precision of the DCC detection and the sufficiency of the DCC data as presented by previous studies [27,28]. Also for the uniformity test, a relaxed threshold value (from 1 K to 2 K) is used to account for the reduced spatial resolution of GEMS. The relaxation of the threshold could make the available data much larger as relatively less affecting to the effectiveness of the DCC detection [28]. The maximum solar and viewing zenith angle are also limited to 40° as the DCC reflectivity significantly changes when the solar and viewing angles are too large [21].

Table 2. DCC detection threshold

Condition	Threshold
IR brightness temperature (TB_{IR})	$TB_{IR} < 205$ K
Spatial uniformity (TB_{IR})	Standard deviation of $TB_{IR} < 2$ K
Spatial uniformity (R_{VIS})	Standard deviation of $R_{VIS} < 0.03$
Solar and viewing zenith angle (θ_0 and θ)	$\theta_0 < 40°$, $\theta < 40°$
GEMS observation area	5°S-45°N, 75°E-145°E

2.2.1. AHI Data Processing

As an input for the DCC detection, AHI measurements are used since the imager on-board GEO satellite provides VIS ($R_{0.47}$) and IR ($TB_{10.4}$) channels with higher temporal resolution while fully covering the TWP region with its full-disk observation (See Table. 3). Since $R_{0.47}$ has higher spatial resolution compared to $TB_{10.4}$, spatially averaged $R_{0.47}$ is prepared. To test the availability of DCCs under the GEMS observation condition, the spatial resolution of GEMS is simulated with each 4 × 4 pixels of the VIS and IR channels and the mean of $TB_{10.4}$ and standard deviation of $R_{0.47}$ and $TB_{10.4}$ are used for the DCC detection.

Table 3. AHI VIS and IR channels for the DCC detection

AHI	**Ch01** ($R_{0.47}$)	**Ch13** ($TB_{10.4}$)
Channel	VIS	IR (window channel)
Wavelength	0.47 µm	10.4 µm
Spatial resolution	1 × 1 km^2	2 × 2 km^2
Observation interval	Every 10 minutes	
Spatial coverage	Full disk scan (nadir at 140.7°)	

2.2.2. Frequency Distribution

A-year long DCC climatology data of AHI from July 2016 to June 2017 are constructed with the spatial grid and sampling frequency matched to the GEMS. In the Asia-Pacific region, most of DCCs are observed at near the tropics and distributed quite evenly over the GEMS observation area, similar to the previous analysis [36–38]. In Figure 1, the spatial distribution also shows a unique arc-shaped boundary which is attributed to the limitation imposed for current study (the viewing zenith angle (θ) should be smaller than 40°). Considering that the viewing zenith angle is a fixed value over time for each pixel of a GEO sensor, the spatial condition might be limited to the pixels satisfying the angle condition.

Figure 2 shows the temporal variation of the number of detected DCCs. In a specific day, most of DCCs are detected at noon time (02:00-04:00 UTC) when the Sun directly passes over the target area. This might be attributed to the constraint of solar zenith angle for the DCC detection as the solar zenith angle is also limited in the same way as the viewing zenith angle. The constraint might also

Peer-reviewed version available at Remote Sens. 2020, 12, 446; doi:10.3390/rs12030446

affect to the seasonal variation along with the seasonal deep convection in the Northern Hemisphere. As shown in Figure 2-(b), DCCs mostly occur from late summer to early autumn over the TWP region since the atmospheric convection is strongly dependent on the abundant moisture and the latent heat accumulated during summertime [37,39–41].

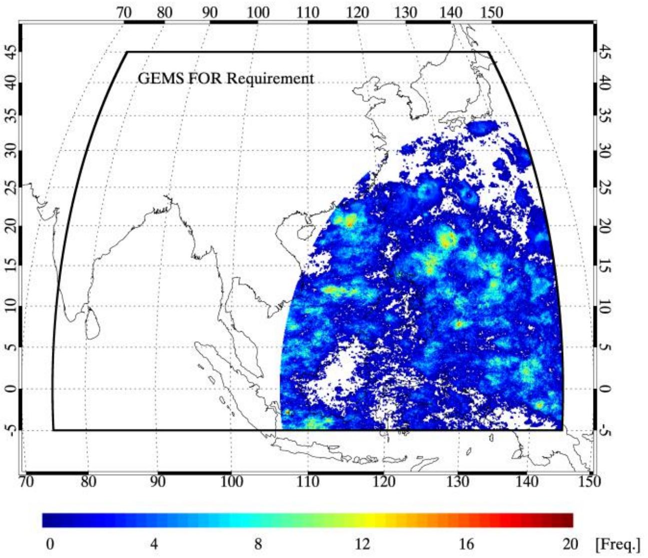

Figure 1. Frequency distribution of DCCs matched to the GEMS FOV over the GEMS observation area with a-year long data of OMI with three days interval for July 2016 – June 2017 (Frequency: the number of DCCs occurred in a year with three days interval)

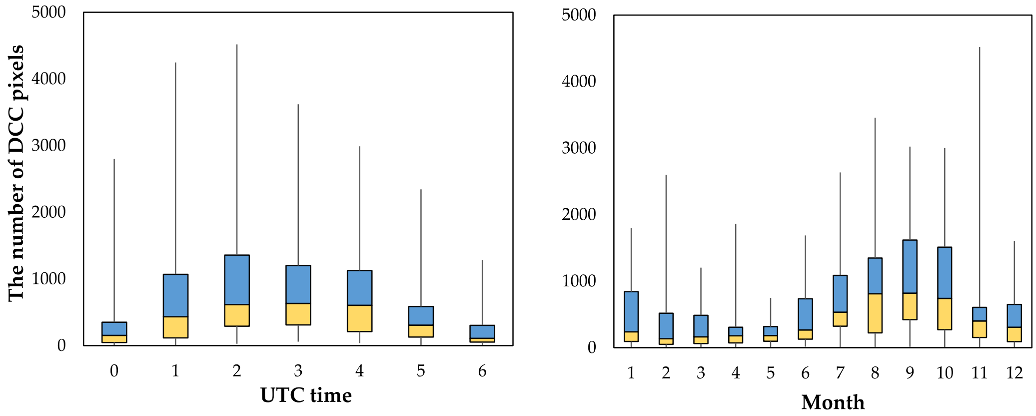

(a) (b)

Figure 2. (a) Hourly and (b) monthly distribution of the number of DCC pixels observed in a single scene over the GEMS observation area corresponding to the GEMS FOV for July 2016-June 2017 (yellow box: from lower quartile to median, blue box: from median to upper quartile)

Even with the limitation imposed by the viewing angular geometry and the seasonality, the average number of DCCs in a single observation scene is still larger than 200 pixels even in the month presenting the minimum frequency. Since GEMS observes the Earth eight times a day, at least over 50,000 DCC pixels could be detected in a month from GEMS when using the conventional DCC detection approach with the collocated AHI data. The number could increase if we use Advanced Meteorological Imager (AMI) onboard GEO-KOMPSAT-2A which is stationed over 128.2°E with its coverage expanding further the western part of AHI.

3. DCC Reflectivity Spectrum

In section 3, DCC reflectivity spectra obtained from OMI and TROPOMI are compared to confirm whether the DCC measurements show similar spectral features and stable signal enough to be compared for the different sensor characteristics and optical paths. In the UV-VIS spectral region, the reflected radiation from ice clouds is largely affected by the angle condition [42] and this makes it important to finely detect DCCs for the accurate characterization of the cloud reflectivity.

3.1. Collocation Process

Since OMI and TROPOMI only cover the UV-VIS and UV-SWIR spectral region, respectively, the DCC detection for both sensors could be performed with the collocated VIS and IR channels of AHI. For the collocation between GEO and LEO sensors, we apply the collocation criteria suggested by the Global Space-based Inter-Calibration System (GSICS) community [43]. Since the collocated data between LEO and GEO are not directly compared in this study, viewing angle is not matched between sensors. As shown in Figure 3, the hyperspectral data satisfying the spatial and angle condition (see Table 2) are collected first and then the AHI VIS and IR channels matching temporal collocation criteria are called. With the collected data, the AHI pixels observing nearly at the same time ($\Delta t < 5$ minutes) with each pixel of OMI and TROPOMI are collocated when the pixels simultaneously satisfy the spatial threshold (located within a half of shorter FOV of a LEO sensor). With the collocated AHI pixels, averaged $TB_{10.4}$ and standard deviation of $TB_{10.4}$ and $R_{0.47}$ are calculated for the DCC detection.

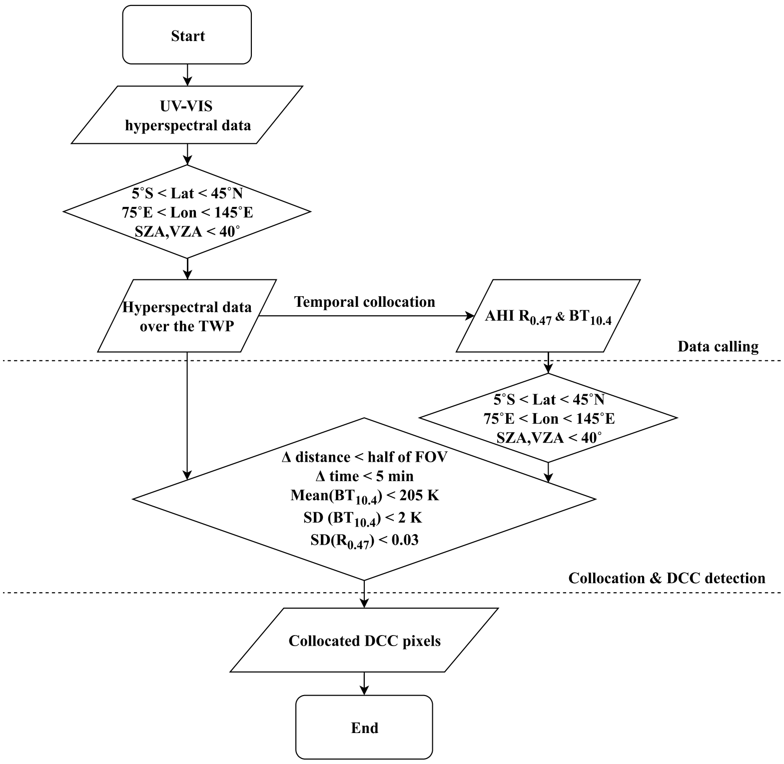

Figure 3. Flow chart of collocation process between UV-VIS hyperspectral sensor and VIS-IR imager for the construction of DCC data

3.2. Apparent Reflectivity of DCCs

GEMS, OMI and TROPOMI provide the spectral radiance data to be used as an input for the retrieval of the geophysical information of the atmosphere. Since the uncertainty in the measured radiance due to the optical path of the instrument could be mitigated by using irradiance which has

Peer-reviewed version available at Remote Sens. 2020, 12, 446; doi:10.3390/rs12030446

the same optical depth [44], here we use reflectivity for the spectral analysis. As OMI and TROPOMI provide solar observation once a day, the timely matched irradiance with the radiance is used for the calculation of the reflectivity. The radiance measured over the DCCs could be written as (by neglecting backscattered radiation by the atmosphere above DCCs);

$$I_\lambda(\theta_0,\theta,\varphi) = R_\lambda(\theta_0,\theta,\varphi)\frac{F_\lambda}{\pi}e^{-\left(\frac{\mu+\mu_0}{\mu\mu_0}\right)\tau_\lambda(z)} \tag{1}$$

Where $I_\lambda(\theta_0,\theta,\varphi)$ is the measured upwelling radiance at wavelength λ with the solar zenith angle θ_0, satellite zenith angle θ, and relative azimuth angle φ. The measured radiance is strongly affected by the cloud reflectivity $R_\lambda(\theta_0,\theta,\varphi)$ and incoming solar irradiance F_λ at the top of atmosphere (TOA) which is attenuated by atmospheric extinction. The atmospheric optical depth $\tau_\lambda(z)$ from the cloud top altitude z to TOA is determined by both absorption and scattering. Here we consider only Rayleigh scattering to make the problem simpler. The angle component μ is cosine of the zenith angle. Thus, the cloud reflectivity using the measured radiance and irradiance can be given as;

$$R_\lambda(\theta_0,\theta,\varphi) = \frac{\pi I_\lambda(\theta_0,\theta,\varphi)}{F_\lambda}e^{\left(\frac{\mu+\mu_0}{\mu\mu_0}\right)\tau_\lambda(z)} \tag{2}$$

Here, the optical depth $\tau_\lambda(z)$ is estimated using an approximation as suggested by Bodhaine et al. [45] considering the altitude and Rayleigh scattering atmosphere. Cloud altitude is approximately set to 16 km since the cloud top of the DCCs nearly reaches to the tropopause at the equatorial region [31,46]. This makes the optical depth of the atmosphere above the clouds in a range of 0.0005-0.0025 from 300 to 500 nm. Since Mie scattering and atmospheric absorption in the upper troposphere are not included in the calculation, the reflectivity is the apparent reflectivity of DCCs, even though it is simply called as the DCC reflectivity in this study.

3.3. Results and Discussion

3.3.1. DCCs Detected for OMI and TROPOMI

Figure 4 shows the DCC pixels identified by OMI and TROPOMI data for a particular cloudy scene (July 3, 2018 06:10 UTC and July 3, 2018 06:40 UTC, respectively). TROPOMI observes the Earth at about 30 minutes earlier than OMI and thus the cloud distributions are slightly different. As shown in the figure, the number of DCC pixels obtained from OMI-AHI collocations is quite smaller than the TROPOMI-AHI collocations. One of the main reasons for the difference is attributed to the lower spatial resolution of OMI. As the size of one OMI pixel is about 15 times larger than that of the TROPOMI, many of the small scale DCCs which are detected as DCCs by TROPOMI data are missed by the OMI because of both threshold test and uniformity test. Because the lower spatial resolution of OMI with the small scale DCC increases not only brightness temperature but also the spatial variability in the IR and VIS making such a pixel as a non-DCC cloud.

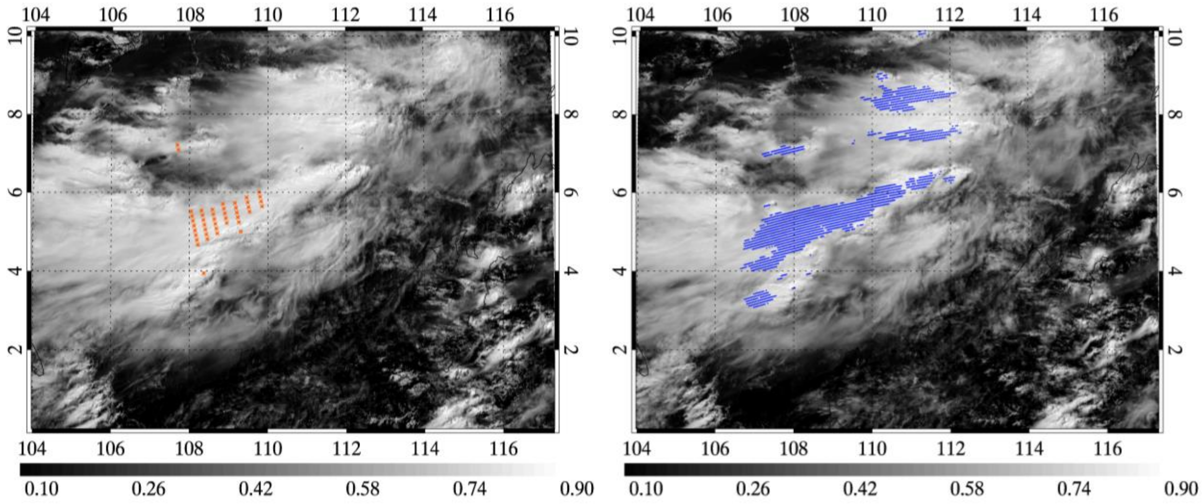

(a) (b)

Figure 4. DCC pixels plotted on AHI $R_{0.47}$ image (a) OMI DCCs on July 3, 2018 06:10 UTC and (b) TROPOMI DCCs on July 3, 2018 06:40 UTC (DCCs marked as orange dots for OMI and blue dots for TROPOMI)

The data quality issues arisen during the long-term operation of OMI also affect to the availability of the OMI observations. For instance, the row anomaly (RA) effect [32] makes nearly a quarter of OMI pixels (especially close to nadir observations) unavailable for the analysis. Figure 5 shows the measured reflectivity of OMI as a function of the position (Row) of the detector (Charge Coupled Device, CCD) and the reflectivity spectrum affected by the RA effect. The measurements in the row number 24-41 contaminated by the RA effect are primarily eliminated during the data processing. However, as shown in the figure 5 (a), the reflectivity at the row numbers close to the nadir port also shows significantly lower reflectivity even though the rows are not flagged as the RA affected pixels. When these observations are detected together as the DCCs, the reflectivity spectrum shows significantly lower value compared to the DCC reflectivity of TROPOMI. Thus, these pixels near the nadir port are also eliminated in this study and it makes the number of DCC pixels of OMI largely reduced. Since the rows close to the nadir port generally have low viewing zenith angle which satisfies the angle condition for the DCC detection, the RA effect significantly affects to the availability of DCC observations of OMI.

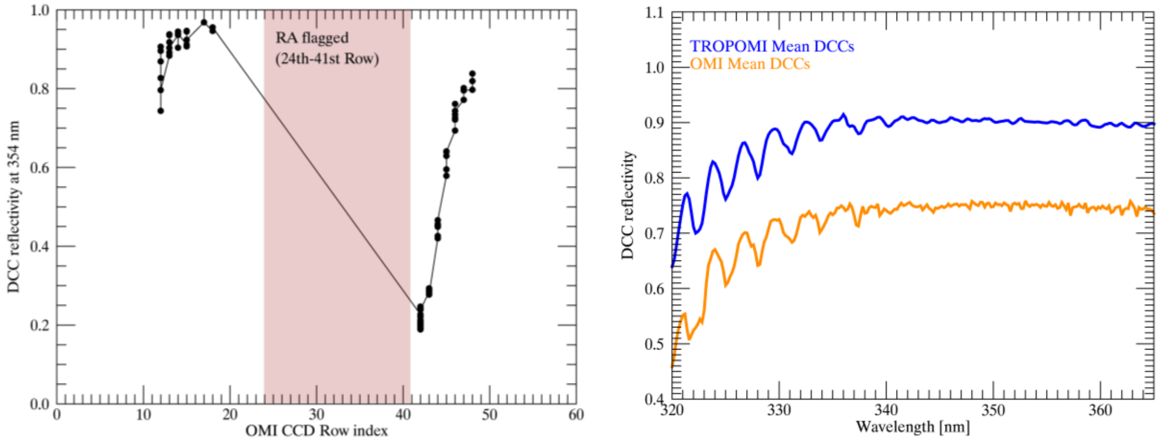

(a) (b)

Figure 5. (a) DCC $R_{0.354}$ binned depending on the position of the detector of OMI (Red box indicates the rows affected by the RA effect) and (b) DCC reflectivity spectrum of OMI (UV-2 product) containing the RA affected observations in the comparison with the TROPOMI DCCs

Peer-reviewed version available at *Remote Sens.* **2020**, *12*, 446; doi:10.3390/rs12030446

3.3.2. DCC Reflectivity Spectrum

The DCC spectra of OMI and TROPOMI observed in a year with ten days interval are presented in Figure 6 showing the mean and standard deviation of radiance and reflectivity at each wavelength. Solar measurements observed on the same day and the scan angle position (the position on the detector) of each DCC measurement are also shown together. Because of the data quality issues as previously mentioned, the number of DCCs for OMI observations in a year is only 3% of the number of TROPOMI. However, even with the distinct difference in the number of measurements, the mean reflectivity of OMI and TROPOMI are almost identical with the higher reflectivity of about 0.9 over the whole wavelength. The DCC spectra also clearly show nearly invariant spectral features except for the both ends of the wavelength range which are attributed to the ozone absorption (300-345 nm) and the pixel saturation of TROPOMI (450-500 nm) [47]. The results indicate that the DCCs observed by the satellite sensor reflect almost stable signal even with the different sensor characteristics, the number of the measurements as well as the observation angle geometry.

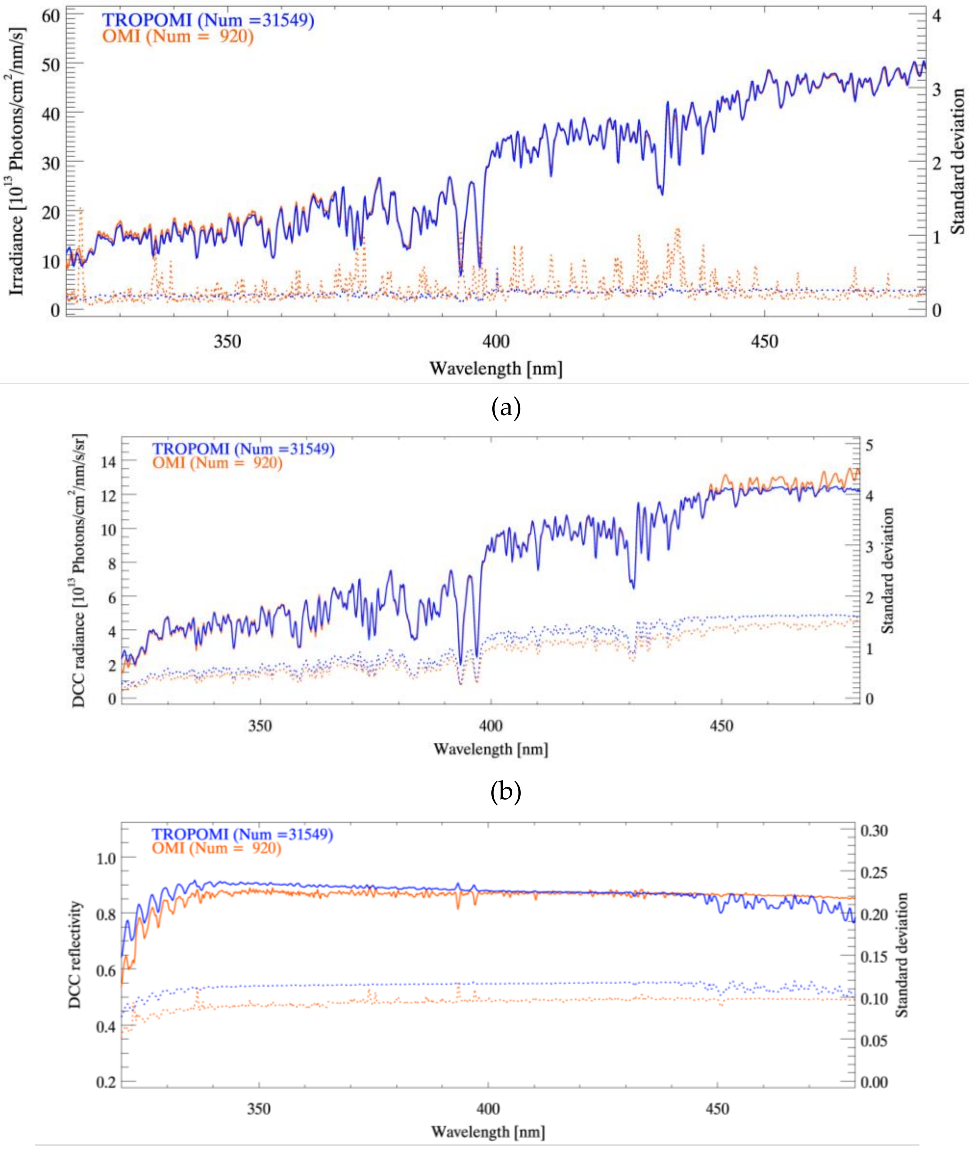

(a)

(b)

(c)

Figure 6. Mean and standard deviation of (a) Irradiance, (b) radiance and (c) reflectivity spectra of OMI and TROPOMI DCCs observed for July 2018 – June 2019 with ten days interval (Solid line: mean and dashed line: standard deviation at each wavelength)

However, some of the differences are also observed between the spectra of OMI and TROPOMI. At shorter wavelength, TROPOMI reflectivity is slightly higher than OMI and as the wavelength increases, the difference becomes much smaller. This might be caused by the diffuser degradation in the solar measurements of TROPOMI since the degradation more significantly occurs at shorter wavelengths. The degradation is to be addressed in the future updates of TROPOMI L1B data in early 2020 as notified by the S5P validation report [47]. TROPOMI DCCs also have smaller spectral noise than OMI since the solar measurements of OMI show higher spectral noise over the whole wavelength as shown in Figure 6 (a). There are also sudden peaks at 393 and 397 nm each corresponding to the Ca II K and Ca II H of Fraunhofer lines, which are caused by the beam-filling effect from the atmosphere above the clouds. As the rotational Raman scattering occurs in the atmosphere, the scattered radiation is also added to the upwelling radiation from the clouds [48]. However, OMI reflectivity shows negative peaks which are seemingly unrealistic considering that the beam filling effect only prominently occurs at the radiance. The unrealistic features may be caused by the unavailable data at particular wavelengths in the OMI irradiance. For the calculation of the reflectivity, the sparse data are approximated by the interpolation which might not properly reproduce the spectral features especially at the deeper peaks.

These results show that TROPOMI still needs further minor updates but the DCC can be a promising target considering the well-matched spectral features with the theoretical background and smaller spectral noises. The abundance of the data also can be an advantage using the measurements for the further study. However, even with the well-explained spectral features, the DCC measurements still have larger systematic difference among the measurements of nearly up to 10% and 12% for OMI and TROPOMI, respectively over the whole wavelength. Since the systematic difference shows increasing trend as the number of the measurements increases, TROPOMI has higher systematic difference compared the OMI. This indicates that as the observation period becomes longer, the dispersion among the DCCs also could significantly increase. The difference might be too large to regard the DCC detection as properly done and this also can make the characterization of the cloud reflectivity quite complicated without knowing the reason of the dispersion. Thus, in Section 4, the thresholds of the conventional DCC detection are tested to reduce the systematic difference among the DCC measurements and improve to finely detect DCC pixels. Since OMI has some of data quality issues, we only use the TROPOMI and AHI observations for the analysis.

4. Improvement of DCC Detection

4.1. Comparison of the VIS and IR Radiation

Figure 7 and 8 show ~~a~~ comparative characteristics of the detected DCCs in the VIS and IR channels used for the DCC detection. The comparison provides us an insight whether the DCC detection is precisely done with the detection of only the colder and brighter cloud cores. Figure 7 shows horizontal distribution of DCCs found over the typhoon Chaba in October 2016. For a one to one comparison, AHI $R_{0.47}$ image is binned to match with the spatial resolution of the $TB_{10.4}$. As shown in Figure 7 (a), DCCs identified as blue dots are mainly found over the typhoon center having cold $TB_{10.4}$ with quite a symmetric distribution around the center. However, Figure 7 (b) presenting detected DCDs over the $R_{0.47}$ image shows an interesting result, as the blue dots over the right side of the typhoon center having lower $R_{0.47}$ of about 0.7. These are the thin cirrus clouds which are spread out from the typhoon center following strong upper air outflows. As these cirrus clouds have colder cloud tops composed of the ice particles, the clouds are detected as DCCs by the conventional detection method, even though the reflectivity is much lower than the actual DCC clouds.

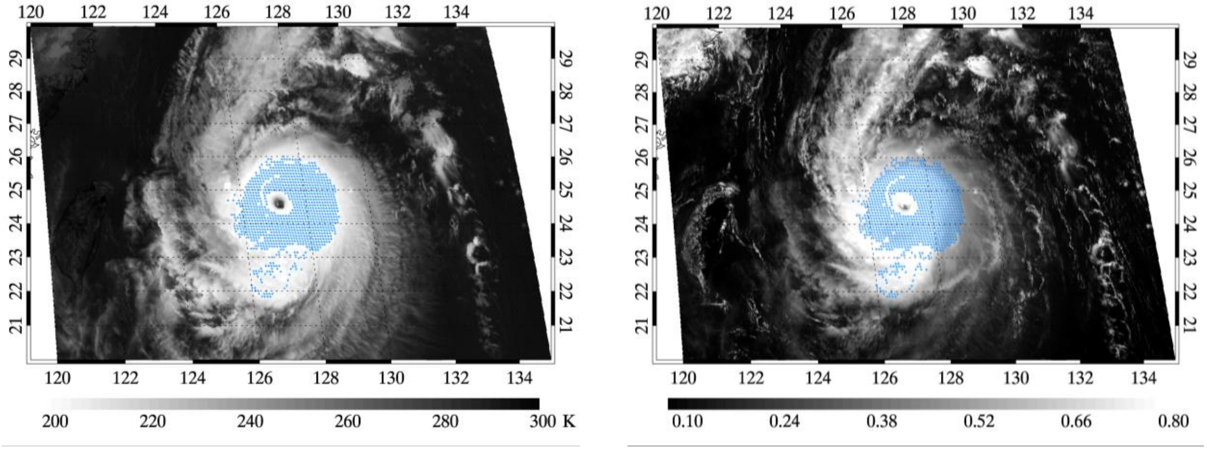

(a) (b)

Figure 7. AHI DCC pixels plotted as blue dots on the (a) 2-km AHI $TB_{10.4}$ and (b) 2-km $R_{0.47}$ images of the typhoon Chaba (October, 3 2016 03:30 UTC)

The difference in the radiative properties of the DCCs between $R_{0.47}$ and $TB_{10.4}$ is also demonstrated in Figure 8 which shows the two-dimensional histogram of $R_{0.47}$ and $TB_{10.4}$ of the detected DCCs. With the histogram, it can be inferred that the increase of $TB_{10.4}$ also increases the skewness in the distribution of $R_{0.47}$. This might be attributed to the increase in the proportion of the clouds having darker reflectivity among the detected DCCs. This also indicates that DCCs usually have colder cloud tops as well as higher reflectivity with the optically thicker vertical structures while the cloud edges and cirrus clouds have similar colder but the darker cloud tops.

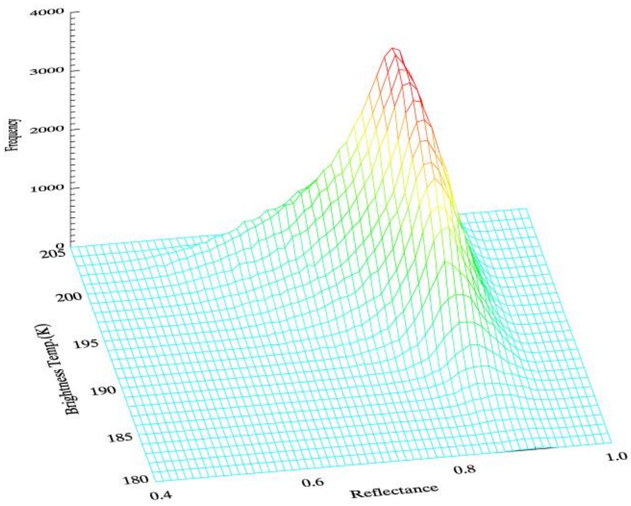

Figure 8. Two-dimensional histogram between AHI $R_{0.47}$ and $TB_{10.4}$ of DCCs over the GEMS observation area using a-year long data of AHI (three days interval) for July 2016-June 2017

These results can be interpreted that the $TB_{10.4}$ threshold might be less effective as a DCC detection threshold especially for the UV-VIS measurements. With only the conventional DCC detection thresholds, it is highly possible that the darker cirrus clouds might be also detected as DCCs. One of few attempts using the DCCs for the monitoring of the UV-VIS hyperspectral sensor also uses only the UV reflectivity threshold for the DCC detection [32]. In the study, the OMI pixels having higher reflectivity at 354 nm ($R_{0.354} > 0.9$) are regarded as DCCs and then used for the monitoring of the temporal stability of radiometric calibration of OMI. Even with such a simple detection, the averaged cloud reflectivity shows a fairly constant value regardless of wavelength (which is the characteristics of DCC reflectivity). Thus, they use the DCC reflectivity for a long term monitoring of the spectral dependence in the sensor performance. However, it was also clear that the DCC reflectivity still showed a seasonal and inter-annual variations which were attributed to the different cloudiness, angle dependence and residual atmospheric effects (refer Figure 32 of [32]). Although it is not easy to quantify, it is highly possible to increase such attributions when the detected DCCs are bright but low lying warm clouds. For example, the optical path for the warm clouds is much longer than the DCCs, causing increased variability of the measured reflectivity due to the increased contribution from the tropospheric air. With the same token, angular variation of the measured reflectivity also increases with increasing optical depth.

For a further clarification of the issues with the warm clouds, Figure 9 and 10 show the spatial distribution of $TB_{10.4}$ and $R_{0.47}$ of the warm clouds and the spectral reflectivity of the clouds having different $TB_{10.4}$ values, respectively. This demonstrates the importance of the IR threshold method for a proper detection of the DCCs especially to select the high altitude clouds which provide homogeneous spectral features with the minimum influence from the troposphere. The blue dots on Figure 9 show the DCC pixels having high reflectivity (TROPOMI $R_{0.354} > 0.9$) with warm IR temperature (AHI $TB_{10.4} > 260$ K). In this case, most of the blue dots are located over the cloud edges having bright reflectivity, although their temperatures are much warmer than the nearby convection core. Thus, if we use the UV-VIS radiation threshold only, it would be difficult to screen out the bright but warm clouds which are close to the cloud cores.

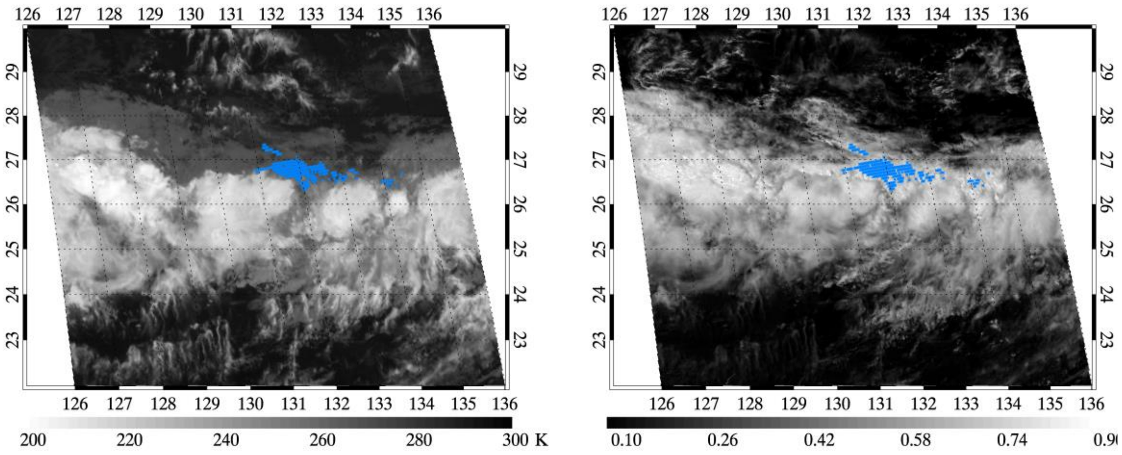

(a) (b)

Figure 9. TROPOMI cloud pixels (AHI $TB_{10.4} > 260$ K, TROPOMI $R_{0.354} > 0.9$) plotted as blue dots on the (a) 2-km AHI $TB_{10.4}$ and (b) 2-km $R_{0.47}$ images (June, 20 2019 04:30 UTC)

Figure 10 shows the reflectivity spectrum of the bright DCCs having different brightness temperatures. Blue line in the Figure 10 (a) shows the averaged reflectivity spectrum of the blue dots shown in Figure 9, while the black line is that of the clouds satisfying the conventional DCC detection thresholds. The reflectivity spectrum (blue line) including the bright but warm clouds clearly shows smaller reflectivity compared to the bright and cold clouds. The different spectral features and increased atmospheric scattering caused by the radiative interactions with the tropospheric atmosphere and the clouds could introduce a significant reduction in the measured reflectivity. The tropospheric effects in the measured reflectivity is further depicted in Figure 10 (b) as the beam filling effects increases the cloud reflectivity with the increased rotational Raman scattering from the tropospheric atmosphere [48]. Thus, Figure 10 shows that the clouds having warmer $TB_{10.4}$ give a lower reflectivity as well as the stronger beam filling effects especially at the Fraunhofer lines compared to the cold clouds. This makes it clear that using both VIS and IR information together could effectively screen out the cirrus and cloud edges as well as detect only colder cloud tops for a better utilization of the DCC reflectivity.

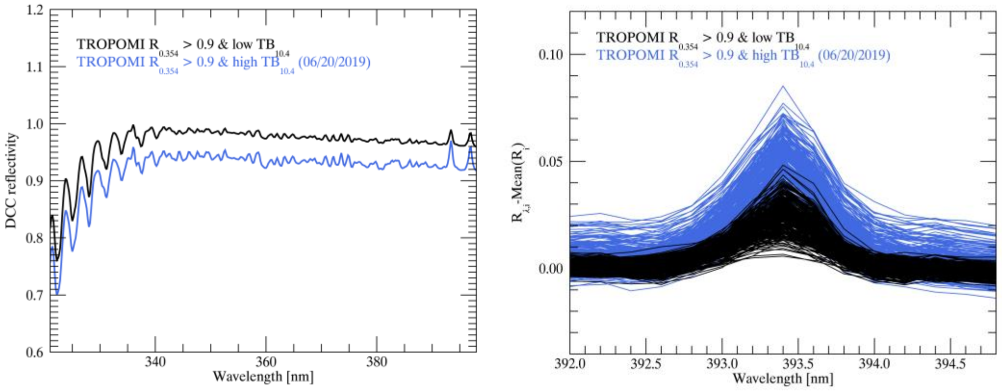

(a) (b)

Figure 10. (a) Mean reflectivity spectrum of TROPOMI DCCs detected by UV reflectivity condition (TROPOMI $R_{0.354}$ > 0.9) and (b) spectral anomaly spectra (i: each DCC pixel, λ: wavelength) in the spectral range of 392.0-394.8 nm (blue line: having low IR temperature and black line: having high IR temperature)

4.2. DCC Detection with the Additional VIS Reflectivity

Based on the previous analysis, we develop an updated DCC detection approach utilizing both reflectivity and brightness temperature. For the inclusion of the reflectivity test, it is important to set a proper threshold value; a tighter threshold for the reflectivity such as 0.9 could produce stable statistics while with the reduced availability of the data, while a relaxed threshold such as 0.6 could increase the data points but increasing variability. This indicates that the optimal threshold of reflectivity for the DCC detection needs to be set weighing both sides, the data availability as well as the stability of the reflectivity distribution. Here, we choose an optimal value by analyzing the variation of statistical parameters as a function of the different threshold values. For the test, AHI $R_{0.47}$ data are used as the reflectivity value since it is independent to the TROPOMI observations.

First of all, Figure 11 (a) and (b) show the frequency distribution of TROPOMI $R_{0.354}$ to the AHI $R_{0.47}$ threshold and the uniformity threshold of AHI $R_{0.47}$ for the DCC detection, respectively. Utilization of $R_{0.354}$ is based on the previous use for OMI study [32] along with the fact that it is less affected by the ozone absorption as well as the directly transmitted light which increases the angle dependence [33]. As shown in Figure 11, application of the AHI $R_{0.47}$ test reduces the speediness of the TROPOMI $R_{0.354}$ distribution and generates a distribution closely following a normal distribution. This is achieved mainly by reducing data located in left tails, the lower reflectivity data. However, some of the left tails still remains since there are residual variations (due to the atmospheric effect above the cloud tops) along with the collocation uncertainty between the AHI and TROPOMI measurements. Since the DCC detection is based on the collocated data between sensors, the possibility for the mis-match between the sensors might increase when the spatial uniformity of a certain cloud is quite lower. Figure 11 (b) also indicates that the cloud pixels having relatively higher spatial inhomogeneity take a large portion in the center of the distribution. This means that the cloud cores vertically shooting up nearly up to the tropopause might have the relatively lower spatial uniformity, which could not be eliminated by the reflectivity threshold. In other words, the TROPOMI $R_{0.354}$ distribution might be closer to a normal as thoroughly detecting only DCCs with a stricter spatial uniformity test as considering the trade-off between the number of data and the stability of the distribution.

Peer-reviewed version available at Remote Sens. 2020, 12, 446; doi:10.3390/rs12030446

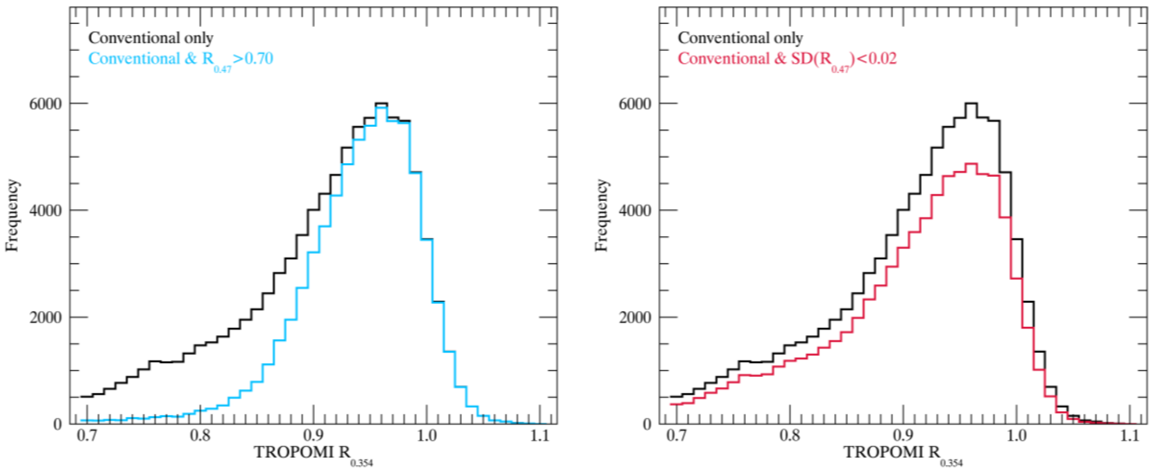

(a) (b)

Figure 11. Frequency distribution of TROPOMI R_{354} with the additional AHI $R_{0.47}$ condition for July 2018 – June 2019 with five days interval

Table 4 shows the statistics of the TROPOMI DCC $R_{0.354}$ by applying different AHI $R_{0.47}$ thresholds to find the effective value which makes the distribution fairly normal without eliminating too many observations. TROPOMI $R_{0.354}$ is also applied together as the detection threshold to reduce the collocation uncertainty by limiting the tail of the distribution to a minimum (TROPOMI $R_{0.354} > 0.7$). Results show that as the AHI $R_{0.47}$ threshold increases, the distribution becomes very close to a normal even though the number of DCCs detected by the thresholds decreases exponentially. Even with the dramatic change of the number of data, the mode of distribution is relatively stable compared to other indicators since the indicator is not significantly affected by the values far away from the center, such as the left tails in this case. Standard deviation of the reflectivity decreases linearly along with the increasing VIS threshold when the kurtosis increases exponentially. Interestingly, only skewness converges at a particular AHI $R_{0.47}$ threshold of 0.64 as having lowest skewness. Since the TROPOMI $R_{0.354}$ reflectivity is skewed to the left because of the darker cirrus having lower reflectivity, skewness of the distribution has a negative value regardless of the AHI $R_{0.47}$ thresholds.

Table 4. Statistics of the TROPOMI DCC $R_{0.354}$ depending on the additional AHI $R_{0.47}$ threshold for the DCC detection with the DCC measurements for July 2018 – June 2019 with five days interval (w/o indicates DCC detection is performed with only the conventional DCC detection thresholds)

AHI $R_{0.47}$	w/o	0.60	0.62	0.64	0.66	0.68	0.70	0.72	0.74	0.76
Count	91630	90752	89861	88286	86138	83569	80475	76696	71469	64857
Mean	0.916	0.917	0.919	0.922	0.925	0.929	0.933	0.938	0.943	0.949
Median	0.932	0.933	0.934	0.936	0.938	0.940	0.943	0.946	0.951	0.956
Mode*	0.960	0.960	0.960	0.960	0.960	0.960	0.960	0.960	0.960	0.960
STD*	0.076	0.074	0.072	0.070	0.067	0.063	0.060	0.057	0.053	0.050
IQR	0.100	0.098	0.096	0.093	0.089	0.084	0.079	0.074	0.068	0.062
Skewness	-0.779	-0.769	-0.765	-0.761	-0.767	-0.780	-0.803	-0.848	-0.917	-1.021
Kurtosis	-0.027	-0.008	0.029	0.110	0.255	0.448	0.706	1.056	1.570	2.225

*Bin size to calculate the mode is set to 0.01. STD and IQR indicate standard deviation and interquartile range.

Table 5 also shows the statistics of the TROPOMI DCC $R_{0.354}$ by applying different threshold for the uniformity test of AHI $R_{0.47}$ to compare the statistics with the previous results. As shown in the Table 5, the central tendency as well as the spread of the distribution only slightly change with the different threshold for the uniformity test of $R_{0.47}$. Kurtosis and skewness might also change as the uniformity increases, even though it does not dramatically change as with the reflectivity threshold.

Table 5. Statistics of the TROPOMI DCC $R_{0.354}$ depending on the uniformity threshold of AHI $R_{0.47}$ for the DCC detection with the DCC measurements for July 2018 – June 2019 with five days interval (w/o indicates DCC detection is performed with only the conventional DCC detection thresholds)

STD* of AHI $R_{0.47}$	w/o	0.025	0.024	0.023	0.022	0.021	0.020	0.019	0.018	0.017
Count	91630	84159	82454	80629	78626	76557	74241	71737	69135	66243
Mean	0.916	0.916	0.916	0.916	0.916	0.916	0.916	0.916	0.916	0.916
Median	0.932	0.933	0.933	0.933	0.933	0.933	0.933	0.932	0.932	0.932
Mode*	0.960	0.960	0.960	0.960	0.960	0.960	0.960	0.960	0.960	0.960
STD*	0.076	0.075	0.075	0.075	0.074	0.074	0.074	0.074	0.074	0.074
IQR	0.100	0.099	0.098	0.098	0.098	0.098	0.097	0.097	0.097	0.097
Skewness	-0.779	-0.788	-0.789	-0.792	-0.793	-0.795	-0.797	-0.796	-0.795	-0.797
Kurtosis	-0.027	-0.002	0.006	0.012	0.017	0.019	0.026	0.025	0.023	0.026

*Bin size to calculate the mode is set to 0.01. STD and IQR indicate standard deviation and interquartile range.

In summary, since the AHI $R_{0.47}$ threshold for the DCC detection largely affects to the left side of the reflectivity distribution of $R_{0.354}$, the skewness might increase with the brighter AHI $R_{0.47}$ threshold until the number of DCCs is decreased by a significant portion. When it comes to the spatial inhomogeneity, some of DCC pixels having relatively low uniformity are eliminated with the stricter uniformity test over the whole range of the TROPOMI $R_{0.354}$, but mostly at the center of the distribution. Since the AHI $R_{0.47}$ threshold as well as the uniformity test might simultaneously affect to the statistics of the reflectivity distribution of TROPOMI $R_{0.354}$, the optimal threshold value for the DCC detection needs to be set considering both effects. Figure 12 (a) and (b) show the number of available DCCs as well as the skewness of the distribution, respectively, as a function of the detection thresholds. Considering the distributions of each variable, the optimal thresholds of each AHI $R_{0.47}$ and the uniformity test for the DCC detection are set to be 0.70 and 0.018, respectively since at the point, the available number of DCCs is still larger even with relatively low skewness of -0.70.

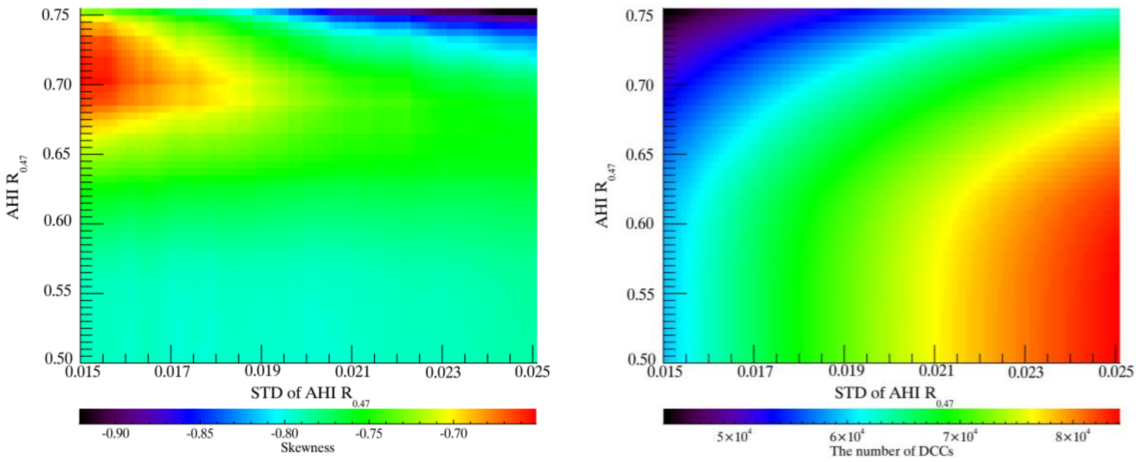

(a) (b)

Figure 12. (a) Skewness and (b) the number of DCCs as a function of the thresholds of AHI $R_{0.47}$ and uniformity test for the DCC detection with the DCC measurements for July 2018 – June 2019 with five days interval

4.3. Verification of the Updated Method

The effects of the updated DCC detection method to the DCC reflectivity spectra would be different for different test. In case of the thermal threshold test, it would be most effective for the screening of the low altitude clouds. Thus, it would decrease the variation of reflectivity by reducing the variations caused by the atmospheric and cloud effects, in this case the warm clouds which have longer optical path lengths. VIS reflectivity also can be a useful indicator to detect only the optically thick clouds which are bright enough to reflect most of the incoming radiation. By using both radiative properties, DCC detection can be further improved to detect only optically thick and very bright cloud targets which show homogeneous spectral features as well as the higher reflectivity with the smaller variation. Figure 13 verifies the advantages applying the updated method for the DCC detection with the threshold values as suggested in the previous section. To clearly show the spectral features of the DCCs depending on the different DCC detection methods, reflectivity spectra at the Fraunhofer line (393 nm, the Ca II K line) are compared together. Figure 13 (a) shows the anomaly spectra of TROPOMI DCCs for the comparison of the beam filling effects. As clear shown, the DCCs detected by the updated DCC detection method present relatively less pointing peak at the Fraunhofer line compared to the DCCs detected with ~~only~~ the reflectivity condition only (TROPOMI $R_{0.354}$). This indicates that the atmosphere above the clouds might be much thinner when the DCCs are detected by the thermal radiation threshold. Figure 13 (b) also presents the comparisons of DCCs detected by the conventional DCC detection method as well as the updated DCC detection. The clouds detected by the updated DCC detection method show relatively higher reflectivity as having lower variability with the standard deviation of about 6%.

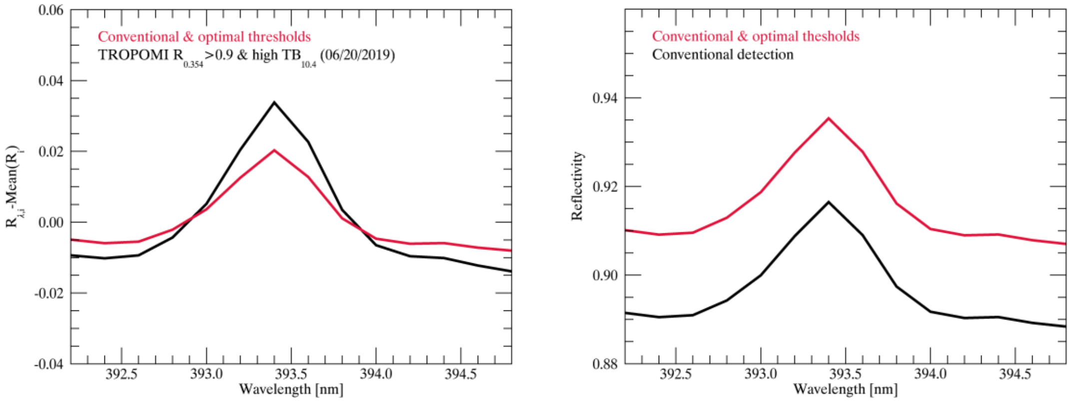

(a) (b)

Figure 13. (a) Spectral anomaly spectra (i: each DCC pixel, λ: wavelength) and (b) reflectivity spectra in the spectral range of 392.0-394.8 nm with the DCC measurements for July 2018 – June 2019 with five days interval (red line: updated DCC detection method and black line in (a): DCCs having high TROPOMI $R_{0.354}$ and high $TB_{10.4}$ and in (b): conventional DCC detection method)

5. Conclusions

As the first UV-VIS hyperspectral sensor onboard GEO satellite, the field of regards of GEMS covers Asia Pacific region including the tropical western pacific (TWP) region. To devise a vicarious calibration approach with the given availability of the calibration targets, in this study, DCCs are tested whether the optically thick clouds provides a stable and bright signal enough to characterize the radiometric calibration of sensors having a different hardware characteristics as well as the observation conditions such as viewing angles, especially in the UV-VIS spectral region. For a feasibility test, VIS and IR channels of advanced himawari imager (AHI) onboard Himawari-8 satellite are used along with the UV-VIS hyperspectral data of OMI and TROPOMI as a surrogate of GEMS. To mitigate the calibration uncertainty caused by degradation and low frequency perturbation of the instrument optical path, the reflectivity (ratio between radiance and irradiance) is used. For a further reduction of uncertainty caused by the observation geometry determined by the satellite and solar zenith angle with the atmospheric effects, the cloud reflectivity derived by considering solar zenith angle, satellite zenith angle, and Rayleigh scattering above the clouds are used for the analysis.

To make sure that the number of DCCs over the GEMS observation area, a-year long AHI data matching the spatial and temporal resolution of GEMS has been analyzed. The detected DCCs using the conventional approach relying on the conventional method, i.e. thermal temperature test and uniformity tests show that DCCs occur with clear seasonality, showing a maximum in September and a minimum in April. It also shows an effect of solar zenith angle during a specific day due to the application of limiting condition in the solar zenith angle to reduce the longer optical path length. Spatially, the viewing zenith angle also limits the availability of DCCs since AHI observes the target area with higher viewing zenith angle compared to GEMS. This limitation with the satellite zenith angle is expected to be improved with the AMI (Advanced Meteorological Imager) onboard GEO-KOMPSAT-2A (GK-2A) which is collocated with GEMS at 128.2° E. Even with such limitations, occurrence of DCCs in a single observation scene shows more than 200 pixels in average which appears to be enough for the statistical approach considering the observation frequency and spatial resolution of GEMS.

Although the number of DCCs detected for OMI and TROPOMI shows a significant difference, mainly due to the poor spatial resolution and degraded data quality of OMI data, the comparison between the estimated spectral reflectivity of DCCs shows comparable results with high reflectivity and weak spectral dependence of reflectivity, even with the disparate sensor characteristics, viewing geometry, and number of data. However, a closer inspection of the reflectivity spectra shows that there is a fairly large variability with the standard deviation of nearly up to 10% which is mainly due to the false DCC detection of thin cirrus which has cold cloud temperature with small optical depth. Furthermore, inspection of an alternative approach, using only reflectivity test for the DCC detection, shows a false detection of warm clouds which have a large reflectivity and lower cloud top altitude. Thus, we devise an updated DCC detection approach using both the thermal and reflectivity tests to screen out cold thin cirrus and bright warm clouds. Based on the variation of statistical parameters of the DCC reflectivity with the different reflectivity threshold value, the threshold value for the reflectivity test is determined to be 0.7 which makes the distribution close to normal and the location values of the distribution converged each other retaining as many observations as possible. However, there are still remaining issues causing the speediness in the reflectivity such as the variations in the cloud properties as well as the angle dependence such as the bidirectional reflectivity distribution of DCCs. The long term variability of DCC reflectivity with the updated detection method are going to be analyzed which could be used to minimize the such variation and to demonstrate applicability of new approach for hyperspectral UV-VIS sensors.

Author Contributions: Myoung-Hwan Ahn designed and supervised the study; Yeeun Lee performed the experiments, analyzed the data, and prepared the manuscript; Mina Kang contributed to the analysis of results. All authors contributed to the edition of the manuscript.

Acknowledgments: This research was supported by Basic Science Research Program through the National Research Foundation of Korea (NRF) funded by the Ministry of Education(2018R1A6A1A08025520) and by Korea Ministry of Environment(MOE) as "Public Technology Program based Environmental Policy (2017000160002).

Conflicts of Interest: The authors declare no conflict of interest.

References

1. Kim, H.-O.; Kim, H.-S.; Lim, H.-S.; Choi, H.-J. Space-Based Earth Observation Activities in South Korea [Space Agencies]. *IEEE Geosci. Remote Sens. Mag.* **2015**, *3*, 34–39.
2. Choi, W.J.; Moon, K.-J.; Yoon, J.; Cho, A.; Kim, S.; Lee, S.; Ko, D. ho; Kim, J.; Ahn, M.H.; Kim, D.-R.; et al. Introducing the geostationary environment monitoring spectrometer. *J. Appl. Remote Sens.* **2019**, *13*, 1.

Preprints (www.preprints.org) | NOT PEER-REVIEWED | Posted: 19 December 2019 doi:10.20944/preprints201912.0260.v1

Peer-reviewed version available at *Remote Sens.* **2020**, *12*, 446; doi:10.3390/rs12030446

3. Veefkind, J.P.; De Leeuw, G.; Stammes, P.; Koelemeijer, R.B.A. Regional distribution of aerosol over land, derived from ATSR-2 and GOME. *Remote Sens. Environ.* **2000**, *74*, 377–386.
4. Wan, Z.; Zhang, Y.; Zhang, Q.; Li, Z. liang Validation of the land-surface temperature products retrieved from terra moderate resolution imaging spectroradiometer data. *Remote Sens. Environ.* **2002**, *83*, 163–180.
5. Boersma, K.F.; Eskes, H.J.; Veefkind, J.P.; Brinksma, E.J.; Van Der A, R.J.; Sneep, M.; Van Den Oord, G.H.J.; Levelt, P.F.; Stammes, P.; Gleason, J.F.; et al. Atmospheric Chemistry and Physics Near-real time retrieval of tropospheric NO 2 from OMI. *Atmos. Chem. Phys* **2007**, *7*, 2103–2118.
6. Gloudemans, A.M.S.; Schrijver, H.; Hasekamp, O.P.; Aben, I. Error analysis for CO and CH_4 total column retrievals from SCIAMACHY 2.3 µm spectra. *Atmos. Chem. Phys.* **2008**, *8*, 3999–4017.
7. Loyola, D.G.; Koukouli, M.E.; Valks, P.; Balis, D.S.; Hao, N.; Van Roozendael, M.; Spurr, R.J.D.; Zimmer, W.; Kiemle, S.; Lerot, C.; et al. The GOME-2 total column ozone product: Retrieval algorithm and ground-based validation. *J. Geophys. Res. Atmos.* **2011**, *116*, 1–11.
8. Yoshida, Y.; Ota, Y.; Eguchi, N.; Kikuchi, N.; Nobuta, K.; Tran, H.; Morino, I.; Yokota, T. Retrieval algorithm for CO_2 and CH_4 column abundances from short-wavelength infrared spectral observations by the Greenhouse gases observing satellite. *Atmos. Meas. Tech.* **2011**, *4*, 717–734.
9. Dinguirard, M.; Slater, P.N. Calibration of space-multispectral imaging sensors: A review. *Remote Sens. Environ.* **1999**, *68*, 194–205.
10. Kowalewski, M.G.; Jaross, G.; Cebula, R.P.; Taylor, S.L.; van den Oord, G.H.J.; Dobber, M.R.; Dirksen, R. Evaluation of the Ozone Monitoring Instrument's pre-launch radiometric calibration using in-flight data. In Proceedings of the Earth Observing Systems X; Butler, J.J., Ed.; SPIE, 2005; Vol. 5882, p. 58820Y.
11. Jaross, G.; Warner, J. Use of Antarctica for validating reflected solar radiation measured by satellite sensors. *J. Geophys. Res. Atmos.* **2008**, *113*, 1–13.
12. Brook, A.; Dor, E. Ben Supervised vicarious calibration (SVC) of hyperspectral remote-sensing data. *Remote Sens. Environ.* **2011**, *115*, 1543–1555.
13. Sterckx, S.; Livens, S.; Adriaensen, S. Rayleigh, Deep Convective Clouds, and Cross-Sensor Desert Vicarious Calibration Validation for the PROBA-V Mission. *IEEE Trans. Geosci. Remote Sens.* **2013**, *51*, 1437–1452.
14. Bhatt, R.; Doelling, D.R.; Wu, A.; Xiong, X.; Scarino, B.R.; Haney, C.O.; Gopalan, A. Initial stability assessment of S-NPP VIIRS reflective solar band calibration using invariant desert and deep convective cloud targets. *Remote Sens.* **2014**, *6*, 2809–2826.
15. Di Giuseppe, F.; Tompkins, A.M. Three-dimensional radiative transfer in tropical deep convective clouds. *J. Geophys. Res. D Atmos.* **2003**, *108*, 4741.
16. Luo, Z.; Liu, G.Y.; Stephens, G.L. CloudSat adding new insight into tropical penetrating convection. *Geophys. Res. Lett.* **2008**, *35*, 2–6.
17. Setvák, M.; Lindsey, D.T.; Rabin, R.M.; Wang, P.K.; Demeterová, A. Indication of water vapor transport into the lower stratosphere above midlatitude convective storms: Meteosat Second Generation satellite observations and radiative transfer model simulations. *Atmos. Res.* **2008**, *89*, 170–180.
18. Fan, J.; Leung, L.R.; Rosenfeld, D.; Chen, Q.; Li, Z.; Zhang, J.; Yan, H. Microphysical effects determine macrophysical response for aerosol impacts on deep convective clouds. *Proc. Natl. Acad. Sci.* **2013**, *110*, E4581–E4590.
19. Loeb, N.G.; Manalo-Smith, N.; Kato, S.; Miller, W.F.; Gupta, S.K.; Minnis, P.; Wielicki, B. a. Angular Distribution Models for Top-of-Atmosphere Radiative Flux Estimation from the Clouds and the Earth's Radiant Energy System Instrument on the Tropical Rainfall Measuring Mission Satellite. Part I: Methodology. *J. Appl. Meteorol.* **2003**, *42*, 240–265.
20. Yongxiang Hu; Wielicki, B.A.; Ping Yang; Stackhouse, P.W.; Lin, B.; Young, D.F. Application of deep convective cloud albedo observation to satellite-based study of the terrestrial atmosphere: monitoring the stability of spaceborne measurements and assessing absorption anomaly. *IEEE Trans. Geosci. Remote Sens.* **2004**, *42*, 2594–2599.
21. Sohn, B.-J.; Ham, S.-H.; Yang, P. Possibility of the Visible-Channel Calibration Using Deep Convective Clouds Overshooting the TTL. *J. Appl. Meteorol. Climatol.* **2009**, *48*, 2271–2283.
22. Bhatt, R.; Doelling, D.; Scarino, B.; Haney, C.; Gopalan, A. Development of Seasonal BRDF Models to Extend the Use of Deep Convective Clouds as Invariant Targets for Satellite SWIR-Band Calibration. *Remote Sens.* **2017**, *9*, 1061.
23. Schmetz, J.; Tjemkes, S.A.; Gube, M.; Van De Berg, L. Monitoring deep convection and convective overshooting with METEOSAT. *Adv. Sp. Res.* **1997**, *19*, 433–441.

24. Doelling, D.R.; Nguyen, L.; Minnis, P. On the use of deep convective clouds to calibrate AVHRR data. In Proceedings of the Earth Observing Systems IX; Barnes, W.L., Butler, J.J., Eds.; 2004; Vol. 5542, p. 281.
25. Minnis, P.; Doelling, D.R.; Nguyen, L.; Miller, W.F.; Chakrapani, V. Assessment of the Visible Channel Calibrations of the VIRS on TRMM and MODIS on Aqua and Terra. *J. Atmos. Ocean. Technol.* **2008**, *25*, 385–400.
26. Doelling, D.; Morstad, D.; Bhatt, R.; Scarino, B. *Algorithm Theoretical Basis Document (ATBD) for Deep Convective Cloud (DCC) technique of calibrating GEO sensors with Aqua-MODIS for GSICS*; 2011;
27. Doelling, D.R.; Morstad, D.; Scarino, B.R.; Bhatt, R.; Gopalan, A. The Characterization of Deep Convective Clouds as an Invariant Calibration Target and as a Visible Calibration Technique. *IEEE Trans. Geosci. Remote Sens.* **2013**, *51*, 1147–1159.
28. Wang, W.; Cao, C. DCC Radiometric Sensitivity to Spatial Resolution, Cluster Size, and LWIR Calibration Bias Based on VIIRS Observations. *J. Atmos. Ocean. Technol.* **2015**, *32*, 48–60.
29. Wang, W.; Cao, C. Monitoring the NOAA operational VIIRS RSB and DNB calibration stability using monthly and semi-monthly deep convective clouds time series. *Remote Sens.* **2016**, *8*, 1–19.
30. Yu, F.; Wu, X. Radiometric inter-calibration between Himawari-8 AHI and S-NPP viirs for the solar reflective bands. *Remote Sens.* **2016**, *8*, 1–16.
31. Ai, Y.; Li, J.; Shi, W.; Schmit, T.J.; Cao, C.; Li, W. Deep convective cloud characterizations from both broadband imager and hyperspectral infrared sounder measurements. *J. Geophys. Res.* **2017**, *122*, 1700–1712.
32. Schenkeveld, V.M.E.; Jaross, G.; Marchenko, S.; Haffner, D.; Kleipool, Q.L.; Rozemeijer, N.C.; Veefkind, J.P.; Levelt, P.F. In-flight performance of the Ozone Monitoring Instrument. *Atmos. Meas. Tech.* **2017**, *10*, 1957–1986.
33. Sneep, M.; de Haan, J.F.; Stammes, P.; Wang, P.; Vanbauce, C.; Joiner, J.; Vasilkov, A.P.; Levelt, P.F. Three-way comparison between OMI and PARASOL cloud pressure products. *J. Geophys. Res.* **2008**, *113*, 1–11.
34. Vasilkov, A.; Joiner, J.; Spurr, R.; Bhartia, P.K.; Levelt, P.; Stephens, G. Evaluation of the OMI cloud pressures derived from rotational Raman scattering by comparisons with other satellite data and radiative transfer simulations. *J. Geophys. Res.* **2008**, *113*, D15S19.
35. Kim, J.; Jeong, U.; Ahn, M.-H.; Kim, J.H.; Park, R.J.; Lee, H.; Song, C.H.; Choi, Y.-S.; Lee, K.-H.; Yoo, J.-M.; et al. New Era of Air Quality Monitoring from Space: Geostationary Environment Monitoring Spectrometer (GEMS). *Bull. Am. Meteorol. Soc.* **2019**, *84*, 00.
36. Hong, G.; Heygster, G.; Miao, J.; Kunzi, K. Detection of tropical deep convective clouds from AMSU-B water vapor channels measurements. *J. Geophys. Res. D Atmos.* **2005**, *110*, 1–15.
37. Liu, C.; Zipser, E.J.; Nesbitt, S.W. Global distribution of tropical deep convection: Different perspectives from TRMM infrared and radar data. *J. Clim.* **2007**, *20*, 489–503.
38. Sassen, K.; Wang, Z.; Liu, D. Cirrus clouds and deep convection in the tropics: Insights from CALIPSO and CloudSat. *J. Geophys. Res.* **2009**, *114*, D00H06.
39. Alcala, C.M.; Dessler, A.E. Observations of deep convection in the tropics using the Tropical Rainfall Measuring Mission (TRMM) precipitation radar. *J. Geophys. Res. Atmos.* **2002**, *107*, 4792.
40. Jiang, J.H.; Wang, B.; Goya, K.; Hocke, K.; Eckermann, S.D.; Ma, J.; Wu, D.L.; Read, W.G. Geographical distribution and interseasonal variability of tropical deep convection: UARS MLS observations and analyses. *J. Geophys. Res. Atmos.* **2004**, *109*, n/a-n/a.
41. Stubenrauch, C.J.; Rossow, W.B.; Kinne, S.; Ackerman, S.; Cesana, G.; Chepfer, H.; Di Girolamo, L.; Getzewich, B.; Guignard, A.; Heidinger, A.; et al. Assessment of Global Cloud Datasets from Satellites: Project and Database Initiated by the GEWEX Radiation Panel. *Bull. Am. Meteorol. Soc.* **2013**, *94*, 1031–1049.
42. Ahmad, Z.; Bhartia, P.K.; Krotkov, N. Spectral properties of backscattered UV radiation in cloudy atmospheres. *J. Geophys. Res. D Atmos.* **2004**, *109*, D01201.
43. Hewison, T.J.; Wu, X.; Yu, F.; Tahara, Y.; Hu, X.; Kim, D.; Koenig, M. GSICS inter-calibration of infrared channels of geostationary imagers using metop/IASI. *IEEE Trans. Geosci. Remote Sens.* **2013**, *51*, 1160–1170.
44. Dobber, M.; Kleipool, Q.; Dirksen, R.; Levelt, P.; Jaross, G.; Taylor, S.; Kelly, T.; Flynn, L.; Leppelmeier, G.; Rozemeijer, N. Validation of Ozone Monitoring Instrument level 1b data products. *J. Geophys. Res.* **2008**, *113*, 1–12.
45. Bodhaine, B.A.; Wood, N.B.; Dutton, E.G.; Slusser, J.R. On Rayleigh optical depth calculations. *J. Atmos. Ocean. Technol.* **1999**, *16*, 1854–1861.
46. Pinto da Silva Neto, C.; Alves Barbosa, H.; Assis Beneti, C.A. A method for convective storm detection using satellite data. *Atmósfera* **2016**, *29*, 343–358.

47. Lambert, J.-C.; Keppens, A.; Hubert, D.; Langerock, B.; Eichmann, K.-U.; Kleipool, Q.; Sneep, M.; Verhoelst, T.; Wagner, T.; Weber, M.; et al. Quarterly Validation Report of the Copernicus Sentinel-5 Precursor Operational Data Products #04: April 2018 - August 2019. **2019**, 1–125.
48. Joiner, J.; Bhartia, P.K.; Cebula, R.P.; Hilsenrath, E.; McPeters, R.D.; Park, H. Rotational Raman scattering (Ring effect) in satellite backscatter ultraviolet measurements. *Appl. Opt.* **1995**, *34*, 4513.